Chemical Engineering Journal 111 (2005) 237–252

Chemical Engineering Journal

www.elsevier.com/locate/cej

Pore-level modeling of isothermal drying of pore networks Effects of gravity and pore shape and size distributions on saturation and transport parameters

Luis A. Segura[1], Pedro G. Toledo*

Chemical Engineering Department and Surface Analysis Laboratory (ASIF), University of Concepción,
PO Box 160-C, Correo 3, Concepción, Chile

Abstract

Simulation results of pore-level drying of non-hygroscopic liquid-wet rigid porous media are presented. 2D and 3D pore networks represent pore spaces. Two kinds of mechanisms are considered: evaporation and drainage. The process is considered under isothermal condition. Of interest here is the drying process when capillary forces dominate over viscous forces; drying is thus considered as a modified form of invasion percolation. Liquid in pore corners allows for hydraulic connection throughout the network at all times. As drying progresses, liquid is replaced by vapor by two fundamental mechanisms, partial-pressure-gradient-driven evaporation and pressure-gradient-driven liquid flow. Using Monte Carlo simulation we find evaporation and drainage times; the shortest calculated indicates the controlling mechanism. Here we report pore-level distributions of liquid and vapor as drying advances. For the calculation of transport properties, details of pore space and displacement are subsumed in pore conductances. Solving for the pressure field in each phase, vapor and liquid, we find a single effective conductance for each phase as a function of liquid saturation. Along with the effective conductance for the liquid-saturated network, the effective permeability of liquid and diffusivity of vapor is calculated. With a Monte Carlo sampling we find optimum network sizes in 2D and 3D to avoid size effects and then investigate the effects of network dimension, pore size distribution, pore shape, and gravity on saturation distributions and effective properties of vapor and liquid.

Keywords: Pore-level drying; Film flow; Drainage; Evaporation; Drying front; Pore size and shape effect; Gravity effect

1. Introduction

Drying is scientifically and technically important. As our conceptual understanding and numerical expertise to simulate complex drying processes increase, the accuracy of simulations hinges on the quality and completeness of input and system parameters. Space limitations prevent us from a complete review of the subject. We limit attention to the main contributions in the area of pore-level modeling of isothermal drying of rigid porous media. Daian and Saliba [1] and Nowicki et al. [2] proposed the first network model to determine macroscopic transport parameters, namely relative permeability of liquid and effective diffusivity of vapor, and their dependency with liquid saturation, distribution of saturation and history of drying. Prat and coworkers first [3–10] and Yortsos and coworkers later [11,12] developed a pore network model of drying combining percolation concepts and calculating diffusive transport of vapor in a gas phase. These two groups studied drying patterns and drying fronts both theoretically and experimentally. Visualization experiments of drying in 2D transparent micromodels are central in identifying pore-level drying mechanisms. Among the first are those of Shaw [13,14]. According to Shaw the drying front develops a highly irregular morphology as it advances and moves by a series of abrupt jumps. He found experimentally that the process of drying can be modeled as a modified form of invasion percolation in which the liquid is removed from the pore structure by counterflow in the same pore segments as the displacing fluid. Pressure gradients that arise from flu-

---

* Corresponding author. Tel.: +56 41 204534; fax: +56 41 247491.
E-mail address: petoledo@udec.cl (P.G. Toledo).

[1] Permanent address: Food Engineering Department, University of Bío-Bío, Chillán, Chile.

1385-8947/$ – see front matter © 2005 Published by Elsevier B.V.
doi:10.1016/j.cej.2005.02.004

ids counterflows stabilize the displacement front even though the displacing fluid is the less viscous of the two fluids. More recently Segura and Toledo [15,16] proposed a pore network model of drying accounting for drainage and evaporation as competing mechanism of liquid removal, liquid wedges flow, and capillary-pressure-gradient-driven shrinkage.

Here we present a mechanistic pore-level model of drying incorporating viscous pressure-gradient-driven flow and partial-pressure-gradient-driven evaporation in 2D and 3D pore networks to determine pore-level distributions of vapor and liquid, drying curves, relative permeability of liquid and relative diffusivity of vapor as function of liquid content. Liquid in pore corners allows for hydraulic connection throughout the network at all times. With a Monte Carlo sampling we find optimum network sizes in 2D and 3D to avoid size effects and then investigate the effects of network dimension, pore size distribution, pore shape, and gravity on saturation distributions and effective properties of vapor and liquid.

The paper is organized as follows. Network model and drying physics are described respectively in Sections 2 and 3. Pore-level vapor and liquid conductances are presented in Section 4. In Section 5 gas and liquid pressure fields are described. In Section 6 macroscopic vapor diffusivity and liquid permeability are presented. The Monte Carlo simulation algorithm is presented in Section 7 and simulation parameters in Section 8. Simulation results are detailed in Section 9. Finally, conclusions are summarized in Section 10.

2. Network model

Porous media are represented by rigid 2D square and 3D cubic networks of cubic pore bodies connected by narrow pore throats with polygonal cross-section circumscribing circles of given radii and depth. Throat radii r_t, or equivalently throat section side half-lengths, are randomly assigned according to probability density functions $f(r_t)$. Pore throat depth h is constant. Pore-body-center to pore-body-center distance L is chosen constant. Pore throat length L_t is constant and equal to a fraction β of L. Pore body side half-length L_b is constant and equal to $(1-\beta)L/2$; body depth is also constant and equal to the throat depth. Fixing the factor β fixes the porosity of the network once $f(r_t)$ and L are set. Fig. 1 illustrates the model and parameters. This network model first presented by Laurindo and Prat [6,7] captures precisely the topology and statistically the geometry of the pore space of a glass micromodel they used to study drying at the pore level; results from these studies we have used to confront our own simulations [15].

3. Drying physics

Initially, the network is fully saturated with liquid. Evaporation takes place by allowing the liquid to evaporate into air from an open edge of the network. At the top of this edge a stream of air and evaporating species mixture flows past slowly. The other edges of the network are considered sealed. Network orientation respect to gravity can be adjusted at will. Menisci movement is considered quasistatic and capillary-controlled. Liquid accumulation in pore corners allows for liquid connectivity throughout the network, no matter how high the capillary pressure is.

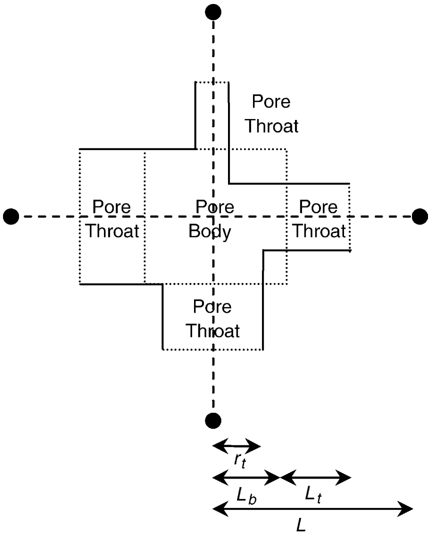

Fig. 1. Pore network and parameters.

The drying front, i.e., the gas–liquid interface, recedes during drying. The process is considered under isothermal condition; thus, mass transfer controls liquid removal. The system is at constant pressure. Drying occurs under no significant external air convection; evaporation rate is thus very low although not necessarily constant. Under these conditions capillary forces are dominant over viscous forces and the drying is considered as a modified form of invasion percolation [17]. Fig. 2 illustrates the events that occur during drying. The initial position of the gas–liquid interface is labeled 1. With drying, in the absence of gravity, the capillary pressure P_c increases and the liquid contained in the largest accessible pore throat, and in corners of already dry throats and bodies,

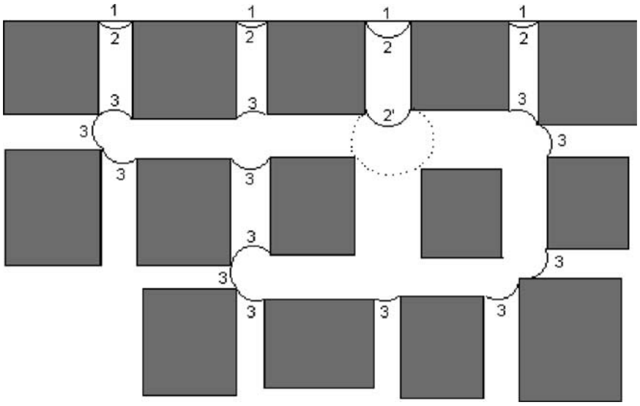

Fig. 2. Schematic representation of the various events that occur during drying.

recedes towards a dry condition, except for liquid wedges in corners. An accessible throat holds a liquid–vapor meniscus. Evaporation drives menisci from their initial flat configuration to configuration 2 such that one meniscus reaches the largest accessible throat, at which

$$P_c = \frac{2\gamma}{r_t}\cos\theta \tag{1a}$$

where r_t is the radius of the largest throat and γ the liquid–air interfacial tension. P_c is defined as $P_g - P_l$, where P_g is the pressure in the gas phase and P_l the pressure in the liquid phase. Locally, at the largest accessible throat, as Fig. 2 shows, the meniscus advances smoothly from configuration 2 to configuration 2′ at constant capillary pressure until it becomes pinned at the opposite edge of that throat. The equilibrium contact angle criterion, however, given by the Young–Dupré equation, does not apply to edges. If other requirements of stability are met, there is a range of contact angles at which the contact line can meet the throat edge. Here, configuration 2′ is considered unstable leading to a Haines jump, a primary trait of fluid interface motion [18]. Menisci move rapidly to new equilibrium positions, accompanied by a sudden pressure drop. After the Haines jump, capillary equilibrium is enforced throughout the network and capillary pressure returns to its prejump value, see configuration 3 in Fig. 2.

In the presence of buoyancy pressure gradients, the capillary pressure varies as a function of height

$$P_c(z) = \frac{2\gamma}{r_t}\cos\theta + \Delta\rho g z \sin\varphi \tag{1b}$$

where the new terms are z the vertical position of a given meniscus from the open edge, g the acceleration due to gravity, φ the network orientation angle respect to gravity, and $\Delta\rho = \rho_l - \rho_v$ is the difference between liquid and vapor densities of the evaporating species. In such a case the pore throat drying first must be accessible and posses the lowest threshold capillary pressure; this pore throat is not necessarily the largest available. In the case of buoyancy, the change in capillary pressure over a distance r is given by $\Delta p_{grav} = \Delta\rho g r$. Taking the ratio of Δp_{grav} and Δp_c, Eq. (1a), gives $B = \Delta\rho g r^2 \sin\varphi/(2\gamma\cos\theta)$. B is called the Bond number, and represents the local interplay between buoyancy and capillary forces.

In a Haines jump, either a sudden local evaporation or a pressure-gradient-driven liquid flow removes liquid in single bodies or assembly of bodies and interconnecting throats. Viscous liquid flow drives liquid to the surface of the network from where evaporation takes place.

Another fundamental event that occurs during drying is fusion of menisci. A throat might hold two back to back menisci. Should capillary pressure rise to the threshold value for that throat, these menisci would coalesce at constant capillary pressure. Evaporation removes liquid in such case.

The mechanism prevailing at any given stage of the drying process is always the fastest, either internal evaporation or drainage and surface evaporation combined. Internal evaporation should prevail if the time required to evaporate the liquid transferred in a jump is less than the combined drainage and surface evaporation times, otherwise drainage should prevail.

When liquid evaporates from throats and bodies, liquid remains at corners allowing for hydraulic connection throughout the network at all times. Liquid volume is V_l and gas volume is V_g. Pore volume of the network is $V\,(V_l + V_g)$. The volume of liquid in the corners of a pore of arbitrary polygonal cross-section is given simply by Bustos and Toledo [19]:

$$V_l = A_w l \tag{2}$$

where

$$A_w = n r_w^2 \left[\sin(\alpha+\theta)\cos(\alpha+\theta) + \frac{\cos^2(\alpha+\theta)}{\tan\alpha} - \frac{\pi}{2} + \alpha + \theta\right] \tag{3}$$

is the cross-section area occupied by liquid; n the number of sides of the polygonal cross-section of the pore; α the pore corner half-angle, which is 45° for square pores; θ the contact angle; r_w the radius of curvature of the longitudinal meniscus define as

$$r_w = \gamma/P_c \tag{4}$$

where γ is interfacial tension and P_c is prevailing capillary pressure; and l the pore segment length, either throat or body. Liquid saturation is calculated as $S_l = V_l/V$.

Internal evaporation or drainage of liquid transferred in a jump, or evaporation in a fusion of menisci, involves a time interval that is simply

$$t = V_H/Q \tag{5}$$

where V_H is the volume transferred. For internal evaporation Q is evaporation rate and for drainage is liquid flow rate. Both flow rates are the result of pore-level flows at the open boundary of the network for drainage or at the vapor–liquid interface for evaporation. It is easy to anticipate that drainage occurs at early times of the drying process when a strongly connected network of liquid, composed of liquid-filled pores and thick liquid wedges in largest pores, exists. Later, when the connectivity of the liquid network weakens, internal evaporation controls the drying process. The development of capillary pressure as menisci turn concave induces shrinkage of the matrix, which contributes to the pressure gradient that drives liquid toward the surface of the network [16].

Liquid driven to the surface of the network by capillary pumping evaporates when air passes over the outer surface of the network. The time involved in this process is also given by Eq. (5), with V_H the volume transferred and Q defined by $Q = k_m A \Delta p$ where k_m is the mass transfer coefficient, A the total area of surface menisci, and Δp the difference between saturation pressure, right above the menisci, and partial pressure of the evaporating species in the outer air stream.

A Haines jump is a dynamic event, involving a complex interplay of viscous, inertia and capillary forces in a complex geometrical-topological environment. Determining the precise pressure fields that develop during a jump requires complex 3D fluid dynamics computations. An attractive simplification emerges when analyzing the pressure trace during a jump. Capillary pressure drops suddenly in a jump, a feature we have used to unravel the structure of porous media by volume-controlled mercury porosimetry [20]; pressure in the gas phase remains constant however and thus liquid builds up pressure locally. Should a high-enough inner pressure gradient develops; capillary pumping of liquid, instead of internal evaporation, should occur. Our simplification involves letting an unstable meniscus, for instance configuration $2'$ in Fig. 1, to loose curvature up to a minimum value when the meniscus touches new pore corners, for instance the dashed meniscus in Fig. 1. Experimental observations, to be published elsewhere, provide partial support to this observation. Stability condition $\mathrm{d}P_\mathrm{c}/\mathrm{d}V_\mathrm{g} < 0$ is not violated in our approximation although pressure, volume and some other constraints are not rigorously considered. This simplification allows us to estimate local liquid pressure increments, account for capillary pumping of liquid, and restrict attention to the sequence of capillary equilibrium states that precede and succeed these jumps. Fusion of menisci occurs at constant capillary pressure and thus pressure-gradient-driven liquid removal is not a possibility, only evaporation. At some time during the drying process, once the liquid network is unable to support viscous flow, mainly thin pores and wedges compose wetting paths to the outer surface, internal evaporation takes place exclusively. We call this a dry regime. Remaining liquid may well be considered hydraulically disconnected and thus conforming isolated liquid clusters or islands of one or more pore segments. Experimental observations of the dry regime reveal that islands closer to the outer surface dry first, when gravity is not a factor. Evaporating an island or a fraction of an island requires a time also given by Eq. (5), where V_H is liquid volume transferred in the drying event and Q is internal evaporation rate. Evaporation from liquid wedges in pore corners represents the last stage of the drying process.

4. Pore-level gas and liquid conductance

Details of pore space and pore occupancy by gas and liquid are subsumed respectively in pore gas and pore liquid conductances such that the volumetric fluid flow q through a given pore is given by

$$q = g\Delta p \tag{6}$$

where g is the conductance of the pore and Δp the pressure drop across the pore. Next, we find pore-level gas and liquid conductances for the various configurations adopted by the two phases.

4.1. Gas conductance

The volumetric flow of an evaporating species through a quiescent gas phase is given by Eq. (6). To define the species diffusive conductance g of each pore segment various gas configurations need to be considered.

i. *Gas at pore center and liquid at pore corners*. When gas occupies the center of a pore and liquid its corners, the pore-level species diffusive conductance in the gas phase is

$$g = AD\frac{M}{dRT}\frac{1}{l} \tag{7}$$

where D is the diffusion coefficient of the evaporating species in the gas phase, M and d respectively the molecular weight and the density of the evaporating species, R the ideal gas constant, and T the temperature. If a given pore throat and connecting pore bodies i and j are all dry and liquid is confined to pore corners, as Fig. 3a shows, then A is the cross-section of the pore space available to gas defined as $A_\mathrm{t} - A_\mathrm{w}$, where A_t is the throat cross-section and A_w the area occupied by liquid as defined in Eq. (3). A is assumed constant along the pore space between pore bodies i and j. l is pore-body-to-pore-body length. Pressure drop across the pore is $\Delta p = P_j - P_i$, where $P_k = \ln(p - p_k)$ with p the total pressure and p_k the species partial pressure at the center of pore body k.

Species diffusive conductances in dry pore bodies with liquid interface, Fig. 3b and c show examples, are also governed by Eq. (6). In calculating the conductance between the center of pore body i and a given meniscus m, A is assumed as the cross-section of the pore space available to gas flow in the pore body, that is $A_\mathrm{b} - A_\mathrm{w}$, where A_b is the body cross-section and A_w the area occupied by liquid as defined in Eq. (3), and l is the distance between the meniscus and the center of the body. Pressure drop across the pore space between the center of the body and the meniscus is $\Delta p = P_\mathrm{t} - P_\mathrm{v}$, where $P_i = \ln(p - p_i)$ with p the total pressure and p_i the species partial pressure at the center of pore body i and $P_\mathrm{v} = \ln(p - p_\mathrm{v})$ with p_v the saturation pressure right above the meniscus.

ii. *Surface meniscus*. The species diffusive conductance for a surface meniscus is simply $g = k_\mathrm{m}A$ where k_m is the mass transfer coefficient and A the meniscus surface area. Fig. 3e shows an example of a surface meniscus. Pressure drop across the pore space between the meniscus and the outer gas is $\Delta p = p_\mathrm{v} - p_\mathrm{ext}$, where p_v and p_ext are respectively the saturation pressure at the meniscus surface and the species partial pressure in the outer gas stream.

iii. *Bridge of liquid*. In this case, there is no gas flow through the pore segment connecting bodies i and j, as Fig. 3b shows, and the gas conductance is set to zero.

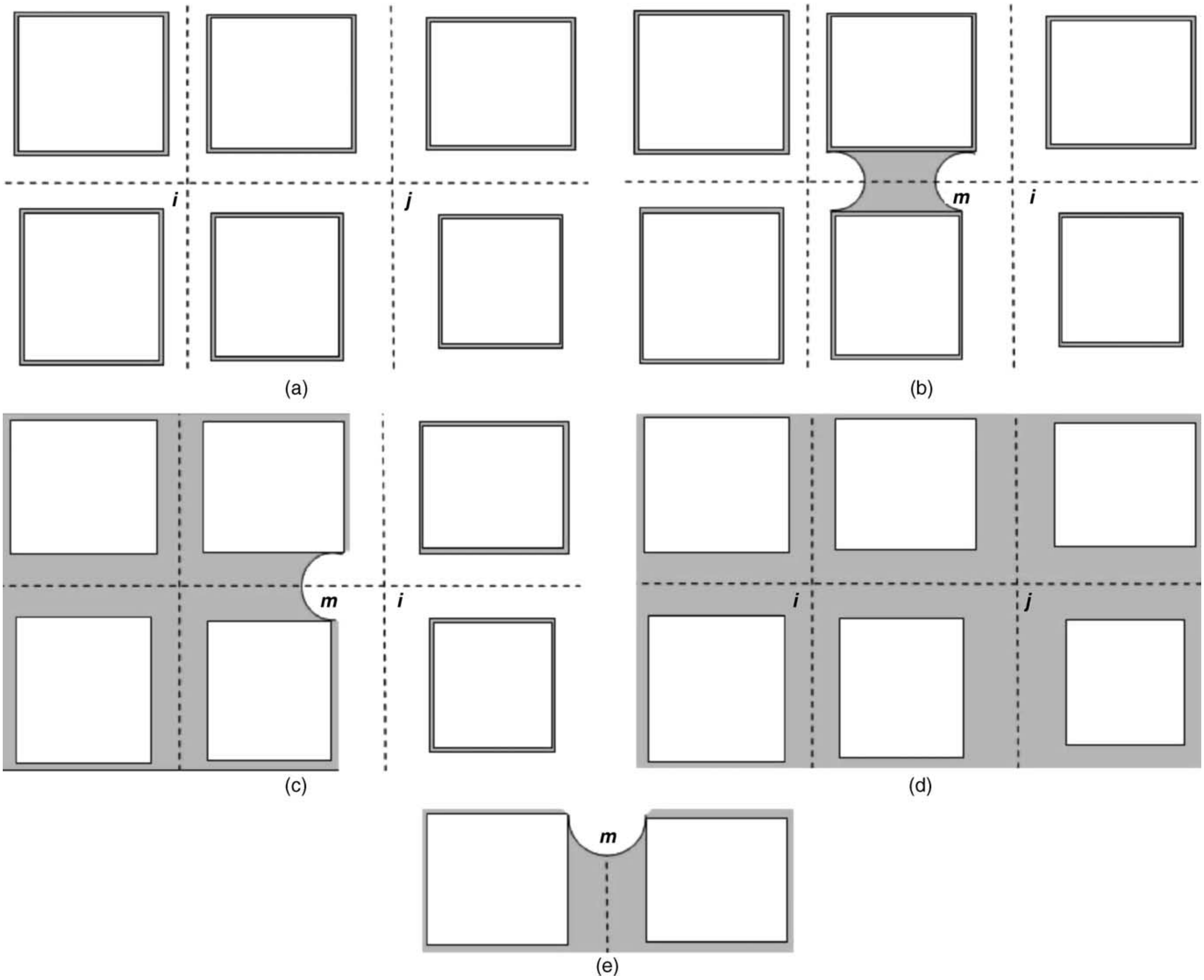

Fig. 3. Pore-level liquid and gas configurations.

4.2. Liquid conductance

Eq. (6) defines the liquid conductance g of each pore segment. Three liquid configurations need to be considered.

i. *Liquid-saturated pore*. For a fully liquid-saturated pore segment, including a throat and adjoining bodies i and j as Fig. 3d shows, the liquid conductance of the pore space is calculated as the harmonic mean of the conductance of throat and bodies [21], that is,

$$\frac{1}{g} = \frac{1}{g_\mathrm{t}} + \frac{1}{2}\left(\frac{1}{g_{\mathrm{b},i}} + \frac{1}{g_{\mathrm{b},j}}\right) \tag{8}$$

where g_b and g_t are conductance of the individual bodies and throat respectively and are given by

$$g = \frac{\pi r_\mathrm{eff}^4}{8\mu_\mathrm{l} l} \tag{9}$$

where μ_l is the liquid viscosity, and r_eff the mean radius between r, either r_t or L_b, and the radius of an effective cylinder of liquid with length l equal to that of the pore, either throat or body, i.e.,

$$r_\mathrm{eff} = \frac{r + \sqrt{A/\pi}}{2} \tag{10}$$

where A is pore cross-section, either throat or body.

ii. *Gas at pore center and liquid at pore corners*. Throat and adjoining bodies hold liquid wedges only. Fig. 3a shows an example. For liquid wedges, the conductance is calculated according to [21]:

$$g = \frac{V_\mathrm{l} r_\mathrm{w}^2}{\eta \mu_\mathrm{l} l^2} \tag{11}$$

where V_l is given by Eq. (2), r_w is given by Eq. (4), and η is a dimensionless resistance factor obtained from the work of [22]. Liquid conductance in this case is calculated as a series array of body–throat–body liquid wedge conductance according to Eq. (8). l is either the length of a throat or a body.

iii. *Liquid bridge*. Adjoining bodies hold liquid wedges. Fig. 3b shows an example. Liquid conductance in this case is calculated as a series array of liquid wedges and bridge conductances. Eq. (11) gives the conductance of liquid wedges of length l. Eq. (9) gives the conductance of a liquid bridge of length l and effective radius given by Eq. (10).

A particular case occurs when one of the adjoining bodies is saturated with liquid. Fig. 3c shows the case. The liquid conductance of the saturated body is given by Eq. (9). The overall liquid conductance is calculated again according to Eq. (8).

5. Gas and liquid pressure fields

Determination of the mechanism prevailing at any stage of the drying process requires calculation of internal evaporation, drainage, and surface evaporation times which require calculation of volumetric flow rates which in turn require calculation of pressure fields both in the liquid and gas phases. Calculations of pressure fields are carried out at the onset of an instability or Haines jump. Fig. 2 is useful to fix ideas. For the pressure field in the liquid phase, configuration 2 and the dashed meniscus, in the largest available throat, are considered. For the pressure field in the gas phase, configuration 2 is considered.

For any given gas–liquid capillary pressure each phase, gas or liquid, develops its own flow network to which conductance can be assigned in much the same way as for single-phase flow. Several approaches are available for computing the pressure fields in either phase once the pore-level saturations are established. Here we use direct solution of nodal material balances for each phase (see for instance [19,23]). A nodal material balance for each phase leads to a system of linear equations, **Gp** = **b**, where **G** is a matrix of conductances, **p** is a vector containing the unknown pressures, and **b** is a vector depending on the pore pressures at the upper and lower boundaries of the network and the conductances of the throats connected to these boundaries. Conductance of a pore segment is zero when a different fluid phase occupies its pore space. For example, in two dimensions for a square network, a typical material balance in a node for a given phase leads to

$$\begin{aligned} &g^X(x,y)P(x-1,y)+g^Y(x,y)P(x,y-1)-[g^X(x,y)\\ &\quad+g^Y(x,y)+g^X(x+1,y)+g^Y(x,y+1)]P(x,y)\\ &\quad+g^X(x+1,y)P(x+1,y)+g^Y(x,y+1)P(x,y+1)=0,\\ &x=1,\ldots,n_X;\ y=1,\ldots,n_Y \end{aligned} \tag{12}$$

where (x, y) represents the position of the node inside the network; $g^X(x, y)$ is the conductance of an X-directed pore segment connecting nodes (x, y) and $(x-1, y)$; $g^Y(x, y)$ is the conductance of a Y-directed pore segment connecting nodes (x, y) and $(x, y-1)$; $P(x, y)$ is the pressure at node (x, y) and n_X and n_Y are the number of nodes in the X and Y directions, respectively.

To find the distribution of nodal pressures in each flow network once an external pressure gradient is imposed we use an iterative solution of the system of equations. The system is optimally stored and solved with a conjugate gradient method with successive overrelaxation. This method is part of the ITPACK routine libraries that are publicly available at the web site http://rene.ma.utexas.edu/CNA/ITPACK. The relaxation parameter is chosen as 1.84.

Boundary conditions for the pressure field in the liquid phase are the corresponding liquid pressures behind each meniscus and the liquid pressure behind the unstable meniscus leading to a jump. For instance consider the case illustrated in Fig. 2. The dashed meniscus, in the largest available throat, when it touches the solid corner has a curvature we approximate as $2/r_{\mathrm{t,m}}$, where $r_{\mathrm{t,m}} = \left(\sum r_{\mathrm{t}}^2\right)^{1/2}$ with the r_{t} corresponding to the two throat radii making up the corner. Capillary pressure drops to $P_{\mathrm{c,min}} = 2\gamma/r_{\mathrm{t,m}}$. Since the gas pressure remains constant and equal to the ambient pressure, the pressure in the liquid phase locally increases up to $P_{\mathrm{l,max}} = P_{\mathrm{c,min}} - P_{\mathrm{g}}$. Boundary conditions for the pressure field in Fig. 2 are thus the liquid pressure behind each meniscus in configurations 2, that is, $P_{\mathrm{l}} = P_{\mathrm{c}} - P_{\mathrm{g}}$, where P_{c} is the prevailing capillary pressure, and $P_{\mathrm{l,max}}$ behind the dashed meniscus. Boundary conditions for the partial pressure field in the gas phase are the saturation pressure, at the temperature of the system, above each meniscus and the partial pressure of the evaporating species in the outside air. Meniscus curvature corrections to the saturation pressure are not considered. With the pressure fields in hand, the flow rates of gas and liquid everywhere are determined, the time needed for internal evaporation, drainage, and surface evaporation are calculated, and the prevailing mechanism for liquid removal in a jump selected. Selecting the correct mechanism is computer intense. Once internal evaporation consistently prevails over drainage, in the dry regime, we use Prat's [3] approach to continue the drying simulation. In an interesting paper Prat [3] calculates the evaporation rate of each liquid island in the medium, in a fashion identical to that described above, and then using Eq. (5) calculates the time needed to dry the largest accessible throat, and adjoining body, in the gas–liquid interface delimiting each island. The shortest time indicates the island to dry. Here we use Prat's [3] criterion only to select the island to dry. To calculate the drying time we use Eq. (5) with Q the evaporation rate of the island and V_{H} the total volume transferred in the process, which according to capillary principles might correspond to a single pore or an assembly of pores; after all an island should remain in capillary equilibrium.

To avoid network size effects we calculate macroscopic parameters, such as vapor diffusivity and liquid permeability, on a central section of the pore networks. In these cases we assign fixed pressures to the upper and lower flow boundaries and use a uniformly increasing pressure as an initial guess.

6. Vapor diffusivity and liquid permeability

With the nodal pressures of a given flow network in hand, the flow rate everywhere is calculated and the network conductance computed from

$$g_j = \frac{Q_j}{P_{\text{in}} - P_{\text{out}}} \tag{13}$$

where g_j is the network fluid conductance of the j phase, Q_j the total flow of phase j throughout the network and $P_{\text{in}} - P_{\text{out}}$ the pressure difference across the central section of the network.

Fick's first law defines the effective diffusivity of the evaporating species in the gas phase:

$$D_{\text{v}} = \frac{Q_{\text{v}}}{A}\left(\frac{RTd}{M}\right)\left(\frac{L}{\Delta p}\right)_{\text{v}} = g_{\text{v}}\left(\frac{RTd}{M}\right)\left(\frac{L}{A}\right) \tag{14}$$

where Q_{v} is the volumetric flow rate of the evaporating species in the gas phase, M and d respectively the molecular weight and density of the evaporating species, R the ideal gas constant, T the temperature, $(\Delta p/L)_{\text{v}}$ the pressure gradient on gas in the direction of the main flow, g_{v} the vapor network conductance, and D_{v} the vapor effective diffusivity. The vapor relative diffusivity, D_{rv}, is defined as $D_{\text{v}}/D_{\text{v}}$ ($S_{\text{l}} = 0\%$).

Darcy's law describes the creeping flow of a single viscous liquid in a porous medium:

$$Q = \frac{k}{\mu}A\frac{\Delta P}{L} \tag{15}$$

where Q is the volumetric flow rate, μ the fluid viscosity, A the cross-sectional area of the porous medium, $\Delta P/L$ the pressure gradient in the direction of flow, and k the intrinsic or absolute permeability. By neglecting any viscous coupling effects and assuming that the simultaneous flow of gas and liquid in a porous medium can be described by Darcy's law one can write for the permeability of the liquid phase

$$k_{\text{l}} = \frac{Q_{\text{l}}}{A}\mu_{\text{l}}\left(\frac{L}{\Delta P}\right)_{\text{l}} = g_{\text{l}}\mu_{\text{l}}\frac{L}{A} \tag{16}$$

where Q_{l} is the volumetric flow rate of liquid, μ_{l} the viscosity of liquid, $(\Delta P/L)_{\text{l}}$ the pressure gradient on liquid in the direction of the main flow, g_{l} the network conductance of liquid, and k_{l} the effective permeability of liquid. The liquid relative permeability, k_{rl}, is defined as $k_{\text{l}}/k_{\text{l}}$ ($S_{\text{l}} = 100\%$).

7. Monte Carlo algorithm

Here we present the sequence of steps and the various parameters used to simulate drying in D-dimensional networks of pore segments with distributed radii.

(a) Specify evaporating species properties such as liquid viscosity, liquid and vapor density and surface tension.
(b) Specify fluid–solid properties such as contact angle.
(c) Choose a lattice of specified dimensions, mean coordination number, and boundary conditions.
(d) Set pore network orientation respect to gravity.
(e) Allow the liquid to evaporate into gas from an open edge of the network. Initially the network is fully saturated with liquid.
(f) Set the evaporating species concentration in the gas stream flowing past at the top of the open edge.
(g) Decorate the underlying lattice with independent pore features. We select rectilinear pore segments with polygonal cross-section and distributed size. Choose pore shape.
(h) Select the parameter β (see Section 2) and the pore-body-center to pore-body-center L.
(i) Set the pore size distribution, this, with β and L, fixes the porosity of the network and also the length of pore throats and size of pore bodies.
(j) Allow capillary pressure to increase, evaporation drives menisci from their initial (previous) configuration, with low curvature, to a new configuration, with higher curvature, where one meniscus, the critical, reaches either the size of the largest accessible throat, in the absence of gravity, or that of the accessible throat having the lowest threshold capillary pressure, in the presence of gravity. Calculate the evaporating species partial pressure field in the gas phase. Boundary conditions are the saturation pressure, at the temperature of the system, above each meniscus and the partial pressure of the evaporating species in the outside gas. With the partial pressure field calculate the evaporation flow rate. Let the critical meniscus advance at constant capillary pressure until it becomes pinned at the throat opposite edge. Calculate the volume of liquid evaporated. Remaining liquid is confined to pore corners in capillary equilibrium and distributed according to pore size and capillary pressure level. With the evaporated liquid volume and the evaporation flow rate calculate the evaporation time. The last configuration with the pinned meniscus is highly unstable leading to a Haines jump. Menisci move rapidly to new equilibrium positions, accompanied by sudden pressure drops. After the jump, capillary equilibrium is recovered throughout the network and the capillary pressure returns to its prejump value. In a jump, either a sudden local partial-pressure-gradient evaporation or a pressure-gradient-driven flow removes liquid in single bodies or assembly of bodies and interconnecting throats.
(k) Determine, according to capillary principles, the local advance of the drying front after a jump, that is, find the new accessible pore throats. At the end of the jump, capillary pressure is at its prejump value. Calculate the liquid volume transferred in a jump. Determine if this liquid volume is transferred by sudden internal evaporation or by drainage to the surface first and evapo-

ration from there then. For internal evaporation, calculate the evaporating species partial pressure field in the gas phase. Boundary conditions are the saturation pressure, at the temperature of the system, above each meniscus, including the pinned meniscus, and the partial pressure of the evaporating species in the outside gas. With the partial pressure field calculate the evaporation flow rate. With the liquid volume transferred in the jump and the evaporation flow rate calculate the evaporation time. For pressure-gradient-driven flow, calculate the pressure field in the liquid phase. Boundary conditions are the liquid pressure behind each meniscus and $P_{\mathrm{l,max}}$, as defined in Section 5, in the throat leading to the jump. With the liquid pressure field calculate the liquid flow rate. With the liquid volume transferred in the jump and the liquid flow rate calculate the drainage time. This liquid evaporates from the outer surface of the network. The time involved is obtained by dividing the liquid volume by the surface evaporation flow rate, as indicated in Section 3. Compare the times required for internal evaporation and for drainage and surface evaporation combined. The shortest indicate the prevailing transferring liquid mechanism.

(l) Notice that fusion of menisci in a single throat may occur, notably at low liquid saturations; evaporation removes liquid in such cases. Remaining liquid is confined to pore corners in capillary equilibrium and distributed according to pore size and capillary pressure level. Calculate the liquid volume transferred in a fusion of menisci. Calculate the evaporating species partial pressure field in the gas phase. Boundary conditions are the saturation pressure, at the temperature of the system, above each meniscus at the beginning of the fusion, and the partial pressure of the evaporating species in the outside gas. With the partial pressure field calculate the evaporation flow rate. With the liquid volume transferred in the fusion and the evaporation flow rate calculate the evaporation time.

(m) Calculate the evaporation rate of each liquid island once internal evaporation consistently prevails over drainage. For each island find the largest accessible throat, in the absence of gravity, or that accessible with the lowest threshold capillary pressure, in the presence of gravity. Thus, each island has a throat that is candidate to experience a jump. For each island (i) determine the local advance of the drying front after the jump, that is, find the new accessible pore throats, capillary pressure is at its prejump value; (ii) calculate the liquid volume transferred in the jump; (iii) calculate the evaporating species partial pressure field in the gas phase, boundary conditions are the saturation pressure, at the temperature of the system, above each meniscus for the initial configuration and the partial pressure of the evaporating species in the outside gas; (iv) with the partial pressure field calculate the evaporation flow rate; and (v) with the liquid volume transferred in the jump and the evaporation flow rate calculate the evaporation time. The shortest time indicates the island drying first.

(n) At the end of a jump or a fusion of menisci, calculate liquid saturation, and liquid and vapor pore-level conductances.

(o) From pore-level conductances, calculate the overall network conductance to both liquid and vapor as a function of liquid saturation. Calculate liquid permeability and vapor diffusivity as a function of condensate saturation. Report liquid relative permeability, and vapor relative diffusivity as function of liquid saturations.

(p) Continue the drying process, steps (j) to (p), until no more liquid remains.

(q) Repeat the simulation, steps (i) to (q), for new samplings of the pore size distribution. Report results with a confidence interval of 95%.

8. Simulation parameters

The mechanistic model of isothermal drying of rigid pore networks is used here to find pore-level distributions of gas–vapor and liquid, drying curves, and corresponding liquid conductivity and vapor diffusivity, and their sensitivities to network size, network dimensionality, network orientation respect to gravity, and pore shape and size distribution. Simulations are run at ambient conditions. The gas phase is air and the evaporating species is hexane. Liquid hexane perfectly wets the solid surfaces and thus contact angle, measured trough the liquid, is zero. Network parameters used in the simulations are given in Table 1. Hexane properties are given in Table 2.

Table 1
Pore network parameters

Description	Value
Porosity, ϕ	0.4
Pore-body to pore-body length, L (μm)	1000
Geometrical parameter, β	0.7746
Throat length, L_t (μm)	774.6
Body half-length, L_b (μm)	112.7
Throat and body depth, h (μm)	1000

Table 2
Hexane properties at ambient conditions: $T = 293.15$ K and $p = 1.013 \times 10^5$ Pa

Description	Value
Molecular weight, M (kg/mol)	86.172
Gas density, d (kg/m^3)	3
Liquid viscosity, μ_l (kg/(m s))	3.26×10^{-4}
Surface tension, γ (N/m)	1.843×10^{-2}
Saturation pressure, p_v (Pa)	16160.57
Partial pressure in outer air, p_{ext} (Pa)	0
Contact angle, θ (°)	0
Diffusivity in air, D (m^2/s)	8×10^{-6}
Mass transfer constant, k_m (kg/(m^2 s))	3.61×10^{-3}

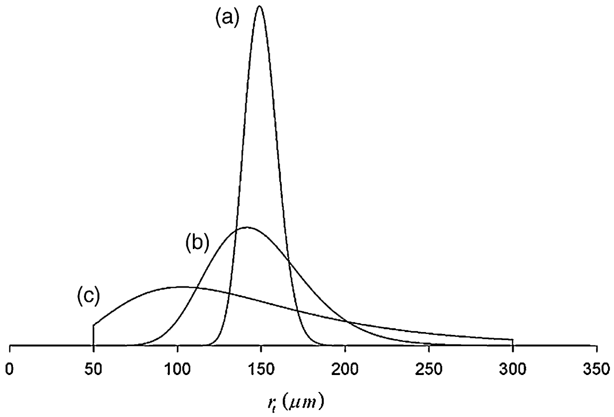

Fig. 4. Truncated log-normal pore throat size distributions.

Pore throat radius is randomly assigned according to the log-normal distribution function

$$f(r_{\rm t}) = \frac{1}{Br_{\rm t}\sqrt{2\pi}} \exp\left[-\frac{1}{2}\left(\frac{\ln(r_{\rm t}) - A}{B}\right)^2\right] \qquad (17)$$

where $\mu = \exp(A + B^2/2)$, $\sigma^2 = \exp(2A + B^2)(\exp[B^2] - 1)$, A and B are adjustable parameters defining mean pore radius, μ, and standard deviation, σ, of the parent normal distributions. Fig. 4 shows the truncated pore size distributions used. Throat radius ranges from 50 to 300 μm. Mean pore radius is 150 μm, standard deviations are $\sigma = 10$ μm (Fig. 4a), $\sigma = 30$ μm (Fig. 4b), and $\sigma = 80$ μm (Fig. 4c).

Pore shapes studied correspond to regular polygons of 3, 4, 5 and 6 sides. Graphical representations of the various shapes are shown in Fig. 5.

To explore the effect of network size on vapor diffusivity and liquid conductivity we use networks of 60 × 60, 80 × 80, 100 × 100, 120 × 120, and 140 × 140 nodes in 2D and 14 × 28 × 14, 15 × 30 × 15, 16 × 32 × 16 and 17 × 34 × 17 nodes in 3D. As expected the variance of both the vapor diffusivity and the liquid permeability, decreases as the size of the network increases. We found that networks of 100 × 100 (20 200 throats) in 2D and 15 × 30 × 15 (21 375 throats) in 3D are enough to minimize network size effects. Drying curves are determined for these optimum-sized networks. In calculating vapor diffusivity and liquid permeability however attention is restricted to a central core of the optimum-sized networks, i.e., a 100 × 50 pore core in 2D and a 15 × 15 × 15 core in 3D. The reduced dimension is along the direction perpendicular to the open side of the networks.

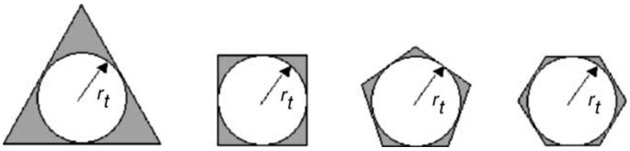

Fig. 5. Graphical representations of the various pore shapes considered.

9. Simulation results

9.1. Pore throat size

Figs. 6–8 show respectively calculated hexane drying curves, liquid relative permeability and vapor relative diffusivity in the 2D and 3D optimum-sized pore networks introduced in Section 7. Fig. 9 shows non-normalized liquid permeability and vapor diffusivity for the optimum-sized 3D pore network. Pore size distributions in Figs. 6–9 are the log-normal distributions shown in Fig. 4. Results correspond to 95% confidence intervals around the mean of four realizations of each pore size distribution. Pore segments are rectilinear with square cross-sections. Pore networks are disposed horizontally and thus gravity is not a factor.

Fig. 6a reveals that not enough liquid remains in the outer surface of the 2D pore networks to produce a constant period of drying. Results for the 3D simulations in Fig. 6b shows a short delay before the fast drying rate period begins. In 3D there is a larger outer surface and capillary pumping drives enough liquid to the surface that evaporation from there controls the early stage of the process. In Fig. 6a and b the transition from drainage to evaporation occurs after 2 and 3 h of drying respectively. The drying curves themselves in Fig. 6 suggest two distinct regimes; a fast drying rate period followed by a significantly slower rate period. Experimental results in transparent micromodels strengthen this perception [5–7]. As others have mentioned [2,6,7,11–14] the fast rate period is a result of viscous pressure-gradient-driven liquid flow that reaches the surface of the network from where evaporation takes place. The slower rate period is a result of evaporation of liquid islands so poorly connected that are unable to sustain liquid flow. Experiments carried out by Laurindo and Prat [6,7] probe the importance of pressure-gradient-driven liquid flow, or capillary pumping, and hydraulic connection through wedges in pore corners. Our pore-level drying model, which incorporates both capillary pumping and evaporation, precisely captures the trend of the experimental data with no significant or sustained departures [15]. The goodness of such fit suggests a right selection of the pore-level drying physics. As expected, the drying curves in Fig. 6 display no significant sensitivity to pore variance and skewness. Dimensionality has a pronounced effect however. Drying is always faster in networks embedded in 3D than in 2D; more strictly, drying is faster in networks with higher connected pore spaces even if they are embedded in the same space dimension.

Liquid hexane relative permeability in Fig. 7 and vapor hexane relative diffusivity in Fig. 8 from both 2D and 3D pore networks show expected trends. As liquid content decreases liquid permeability decreases and vapor diffusivity increases.

Liquid relative permeability approaches a typical s-shaped form. Permeability is high at high saturations of the liquid phase. Permeability decreases abruptly once mainly small-saturated pores and liquid wedges composed liquid saturation. The inflection point in the permeability marks the point where wedges of liquid control its conductivity; at this point

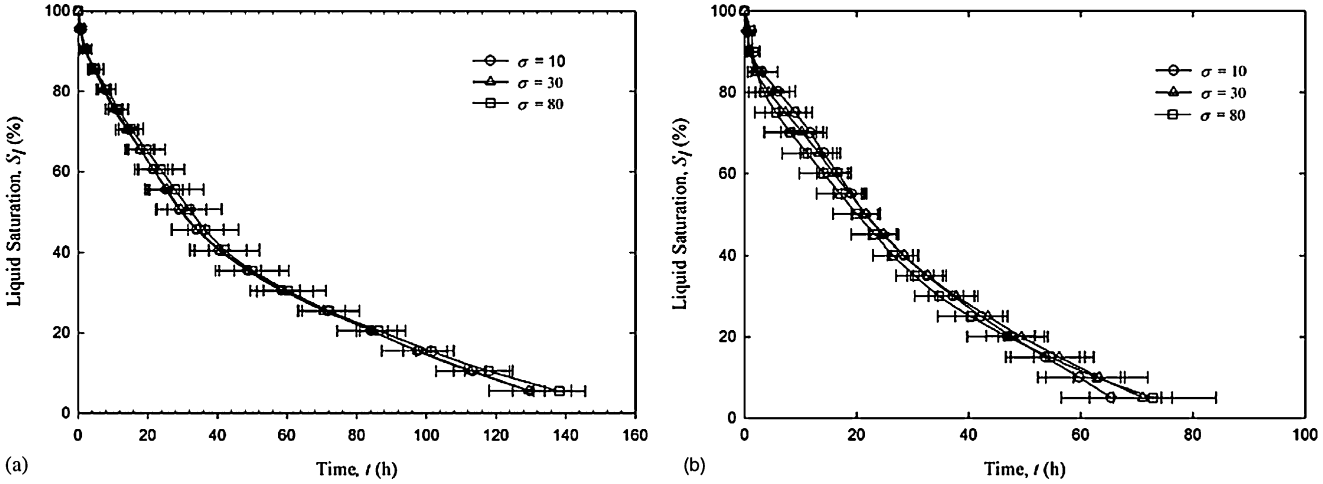

Fig. 6. Pore size variance and skewness effect on simulated drying curves in pore networks saturated with hexane: (a) 2D 100 × l00-pore networks, (b) 3D 15 × 30 × l5-pore networks. Pore segments with square cross-section.

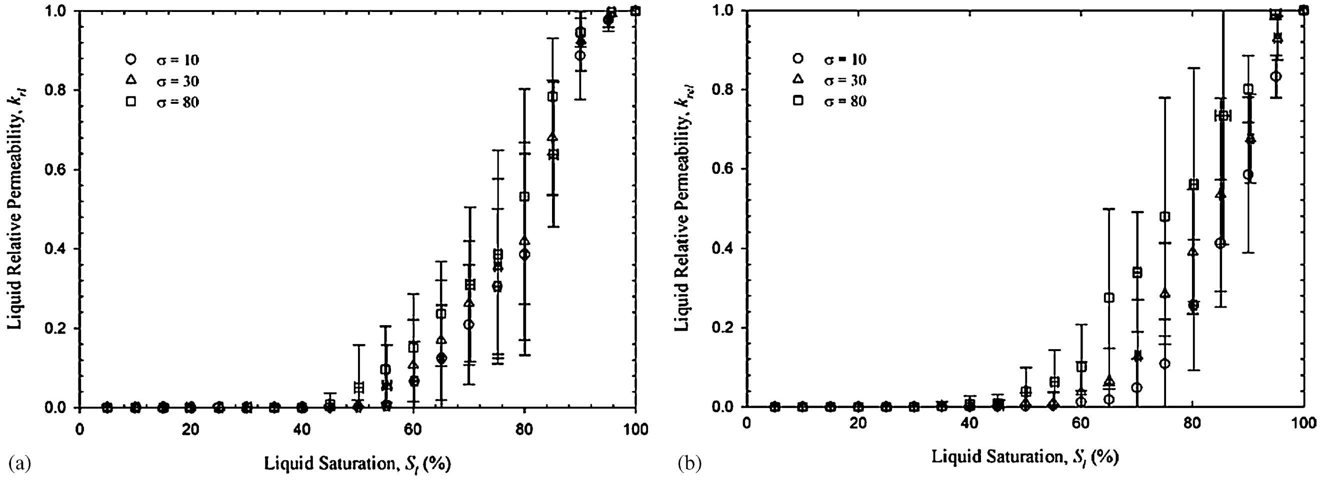

Fig. 7. Pore size variance and skewness effect on vapor hexane relative diffusivity in pore networks: (a) 2D 100 × 100 pore networks, (b) 3D 15 × 30 × 15 pore networks. Pore segments with square cross-section.

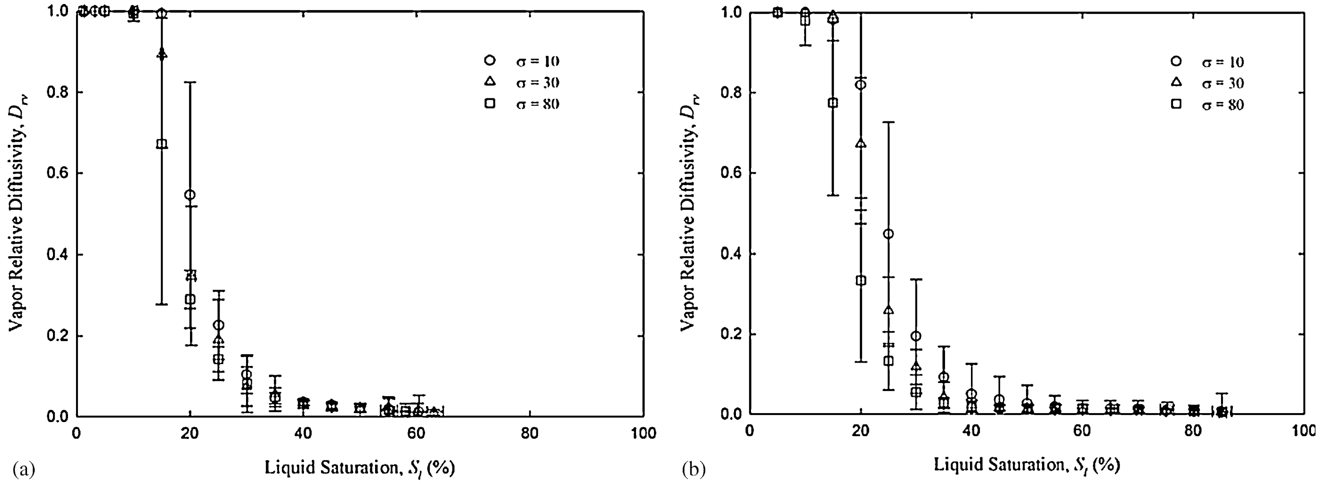

Fig. 8. Pore size variance and skewness effect on liquid hexane relative permeability in pore networks: (a) 2D 100 × 100 pore networks, (b) 3D 15 × 30 × 15 pore networks. Pore segments with square cross-section.

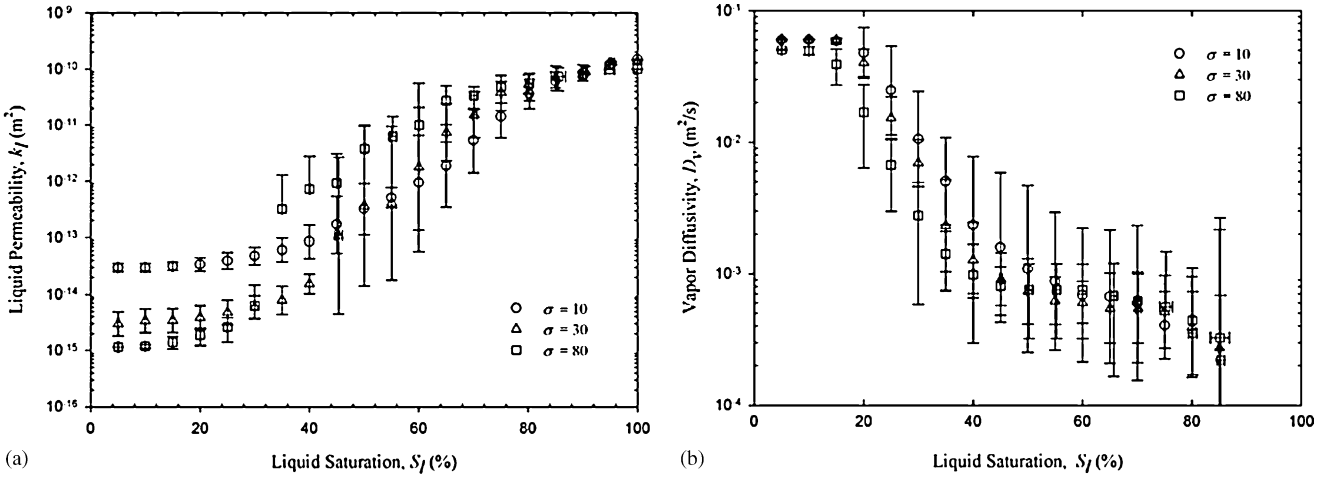

Fig. 9. Pore size variance and skewness effect on (a) liquid hexane permeability and (b) vapor hexane diffusivity in 3D 15 × 30 × 15 pore networks. Pore segments with square cross-section.

the liquid network is unable to sustain significant liquid flow. The permeability of liquid hexane shown in Fig. 9a for 3D networks exhibits little sensitivity to pore size variance and/or skewness at high liquid saturations. A strong liquid-saturated pore network exists. As liquid saturation decreases a pronounced spread of the liquid permeability is observed as the pore size variance and/or skewness changes, see also Fig. 7. At any given high saturation in Fig. 9a the higher the variance and/or skewness in pore size the higher the liquid permeability. The effect of the skewness is even more pronounced than the effect of the variance of the pore size distribution. In all cases of variance and/or skewness, the larger pore segments, available in larger number in pore populations with higher variance and/or skewness, control de conductance of the liquid network. The situation is the opposite at lower saturations, which is of course not evident when the liquid permeability is reported normalized as relative permeability. At any given saturation, in the low saturation range, the higher the variance and/or skewness in pore size the lower the liquid permeability. Again, the effect of the skewness is even more pronounced than the effect of the variance of the pore size distribution. In all cases of variance and/or skewness, the smaller pore segments, available in larger number in pore populations with higher variance and/or skewness, control de conductance of the liquid network. Large pore segments saturated with liquid merely act as liquid connectors.

According to Figs. 8 and 9b, vapor hexane diffusivity in 2D and 3D approaches an inverted s-shaped form, rising abruptly once a cluster of hexane vapor traverses the network for the first time. Then diffusivity increases smoothly as liquid saturation decreases. Vapor diffusivity is nil for liquid saturations high enough. At some liquid saturation, higher in 3D than in 2D, a sort of percolation threshold of sample-spanning paths of vapor-filled pore segments is reached and the vapor diffusivity reaches a small steady non-zero value. As liquid saturation decreases, vapor diffusivity increases slowly both in 2D and in 3D. For liquid saturations in the medium range, as large populations of pore segments become dry, the vapor diffusivity increases faster, abruptly both in 2D and in 3D. At low enough saturations, liquid hexane exists mainly as liquid wedges in pore corners; vapor diffusivity recovers a low increasing pace, as liquid wedges become thinner, before reaching its highest value. Figs. 8 and 9b show that at high-enough liquid saturations, the vapor diffusivity displays no significant sensitivity to the variance and skewness of the pore size distribution. However, the same figures show that the impact of pore size variance and skewness is significant at low liquid saturations (below 50%). For these saturation regimes, at any given liquid saturation, the lower the variance and/or the skewness in pore size the higher the vapor diffusivity. The skewness effect being more pronounced. Pore networks decorated with pore size distributions exhibiting high pore size variance and/or skewness attain given saturations with larger populations of small liquid-saturated pore segments as compared with distributions having low pore size variance and/or skewness. At low saturations of liquid hexane, pore segments holding liquid wedges in corners control de diffusivity of hexane vapor. Figs. 8 and 9b show that in this saturation regime, the vapor diffusivity displays no significant sensitivity to the variance and/or skewness of the pore size distribution.

9.2. *Pore shape*

Figs. 10–12 show respectively calculated hexane drying curves, liquid relative permeability and vapor relative diffusivity in the 2D and 3D optimum-sized pore networks introduced in Section 7. Fig. 13 shows non-normalized liquid permeability and vapor diffusivity for the optimum-sized 3D pore network. Pore size distribution in Figs. 10–13 is the log-normal shown in Fig. 4c. Results correspond to 95% confidence intervals around the mean of four realizations of the pore size distribution. Pore segments are rectilinear with triangular, square, pentagonal and hexagonal cross-sections. Again pore networks are disposed horizontally and thus grav-

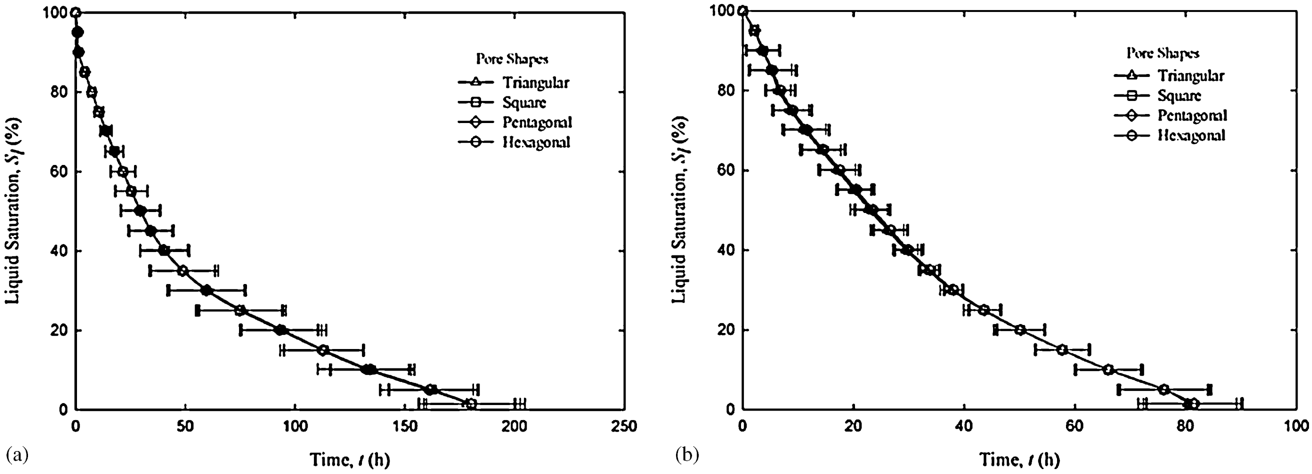

(a) (b)

Fig. 10. Pore shape effect on simulated drying curves in pore networks saturated with hexane: (a) 2D 100 × 100 pore networks, (b) 3D 15 × 30 × 15 pore networks. Pore size distribution is shown in Fig. 4e.

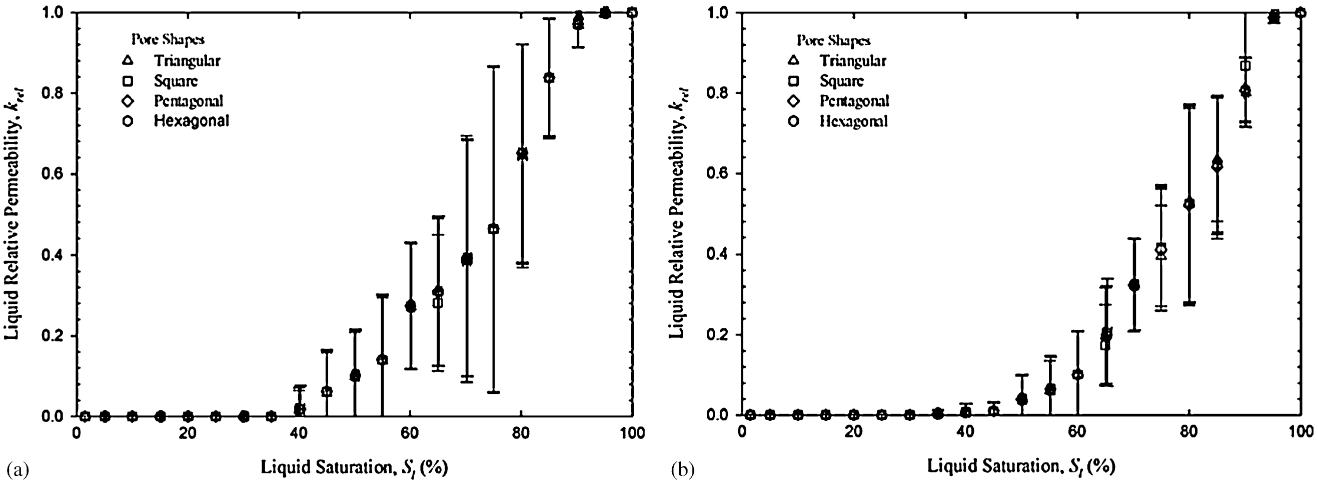

(a) (b)

Fig. 11. Pore shape effect on vapor hexane relative diffusivity in pore networks: (a) 2D 100 × 100 pore networks, (b) 3D 15 × 30 × 15 pore networks. Pore shape effect. Pore size distribution is shown in Fig. 4e.

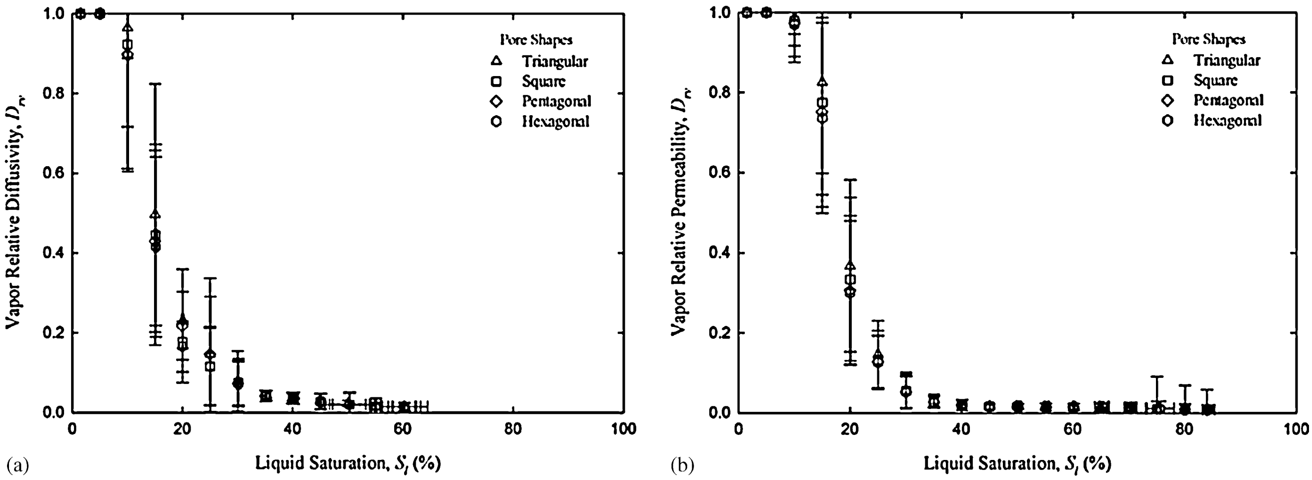

(a) (b)

Fig. 12. Pore shape effect on liquid hexane relative permeability in pore networks: (a) 2D 100 × 100 pore networks, (b) 3D 15 × 30 × 15 pore networks. Pore shape effect. Pore size distribution is shown in Fig. 4e.

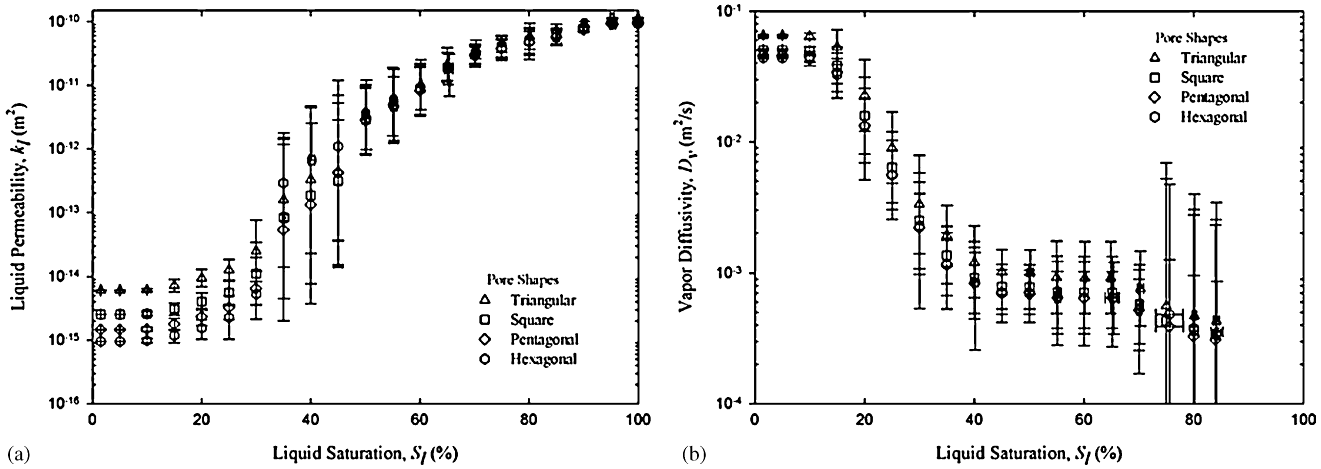

Fig. 13. Pore shape effect on (a) liquid hexane permeability and (b) vapor hexane diffusivity in 3D 15 × 30 × 15 pore networks. Pore size distribution is shown in Fig. 4e.

ity plays no role. As expected, the drying curves, vapor relative diffusivity and liquid relative permeability display a pronounced dependence on the dimensionality of the embedding space and a clear insensitivity to pore shape. Again, drying is faster in networks with higher connected pore spaces. In Fig. 10a and b drainage switches to evaporation after 1.4 and 4 h of drying respectively.

Fig. 13a and b however reveal respectively that non-normalized liquid permeability and vapor diffusivity in 3D networks show some sensitivity to pore shapes. However, the overall shapes of the curves are maintained. For a given pore size distribution and liquid saturation, Fig. 13a and b reveals that liquid permeability and vapor diffusivity are higher in networks with pore segments showing higher angularity such as the triangular pores. Triangular pore segments, circumscribing circles of the same radius as lower angularity pores, remain open to vapor flow at higher liquid saturations than do less angular pores. At any given capillary pressure, less angular pore segments built liquid bridges with lower liquid saturations. Thus for any given liquid saturation the higher the pore angularity the higher the probability of finding pores open to vapor flow. This explains the higher vapor diffusivities observed in Fig. 13b in triangular pore segments respect to the other higher-sided pore segments. However, lower-sided pores open to gas flow maintain higher corner liquid inventories and thus liquid remains more fully and strongly connected than in higher-sided pores. This explains the higher liquid permeability observed in Fig. 13a in triangular pore segments respect to higher-sided pores. The situation is particularly clear at low liquid saturations when liquid recedes mostly in pore corners and tiny pores; triangular pores built thicker liquid wedges and thus liquid permeability is higher.

9.3. Gravity

Fig. 14 displays the effect of gravity on saturation distribution and drying fronts in 2D 100 × 100 pore networks. Fig. 15 displays the effect of gravity on the drying curves of the 2D and 3D optimum-sized pore networks introduced in Section 7. Fig. 16 displays the effect of gravity on non-normalized liquid permeability and vapor diffusivity for the optimum-sized 3D pore network. Pore size distribution in Figs. 14–16 is the log-normal shown in Fig. 4c. Results in Figs. 15 and 16 correspond to 95% confidence intervals around the mean of four realizations of the pore size distribution. Pore segments are rectilinear with square cross-section. Pore networks are disposed in three different ways respect to gravity (1) horizontally $\varphi = 0°$, gravity plays no role, $g = 0$ and thus $B = 0$, (2) inclined, with the open side upwards, $\varphi = 87.02°$, $g > 0$ and thus $B = 0.35$, and (3) inclined, with the open side downwards, $\varphi = -3.6°$, $g < 0$ and thus $B = -0.022$. The angle φ is measured respect to the horizontal.

Fig. 14 shows a comparison of simulated morphologies of drying fronts affected variously by gravity at equivalent liquid saturations. Drying fronts in the images move from top to bottom. Pores filled with hexane vapor are shown in black; regions filled with liquid hexane are shown in white. Left and right boundaries are sealed. The leftmost column in Fig. 14 displays a sequence of saturation maps and drying fronts for the case $g = 0$. The sequence shows that at early stages of the process, when the average velocity of the drying front is high, a roughly compact front forms. As the front velocity slows, the size of the front roughness increases and capillary fingers develop. Islands of liquid of various sizes appear. Notable is the compact front that evolves behind the rough front. Similar analysis has been offered first by Shaw [13,14] and then by Laurindo and Prat [6,7]. Important is the striking resemblance of the simulated drying pattern when compared to experimental patterns at the same drying times [13–15]. According to the model, the drying pattern at the beginning of the process is determined by drainage, or capillary pumping, then by the interplay between drainage and evaporation, and later, when only islands of liquid remain, by evaporation. From here on, by drainage

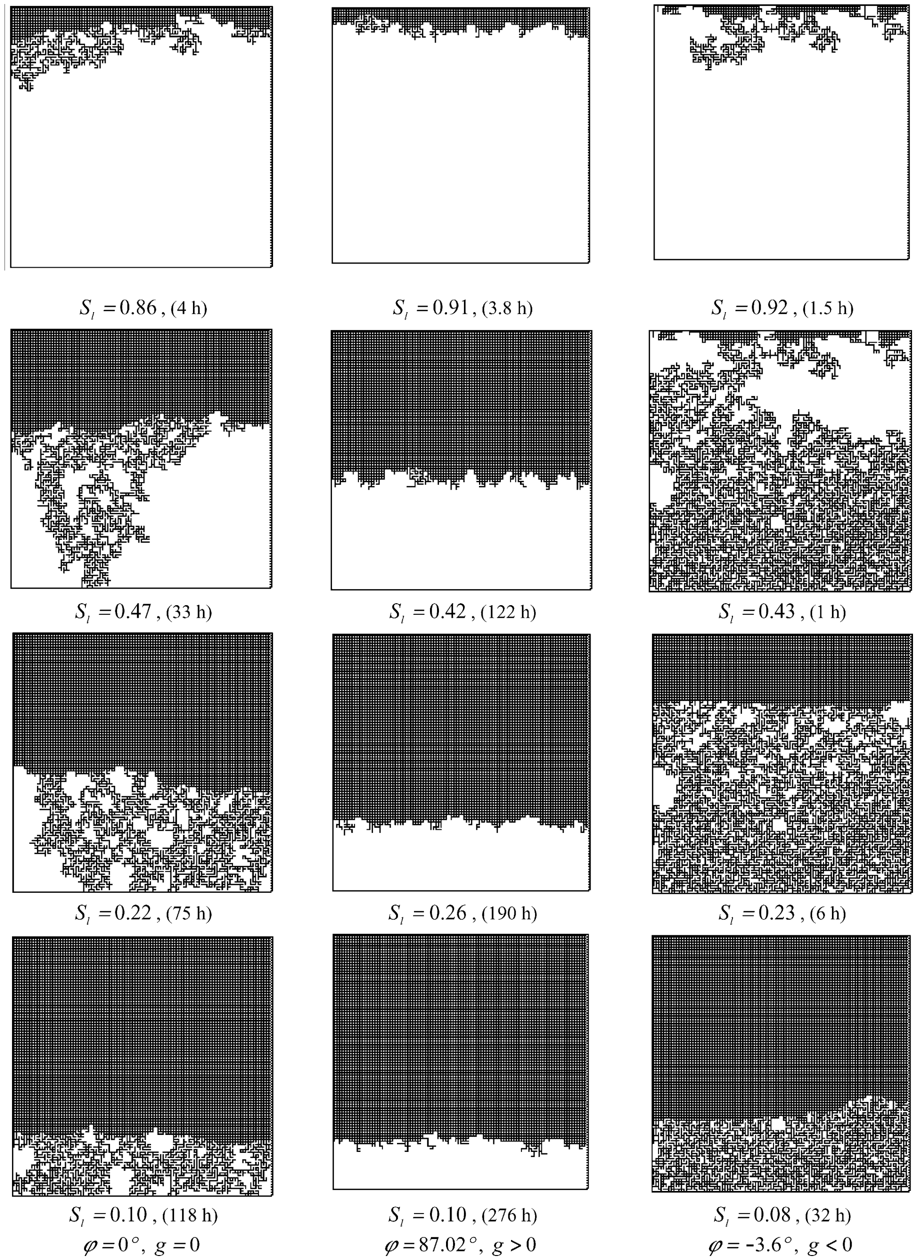

$S_l = 0.86$, (4 h) $S_l = 0.91$, (3.8 h) $S_l = 0.92$, (1.5 h)

$S_l = 0.47$, (33 h) $S_l = 0.42$, (122 h) $S_l = 0.43$, (1 h)

$S_l = 0.22$, (75 h) $S_l = 0.26$, (190 h) $S_l = 0.23$, (6 h)

$S_l = 0.10$, (118 h) $S_l = 0.10$, (276 h) $S_l = 0.08$, (32 h)

$\varphi = 0°,\ g = 0$ $\varphi = 87.02°,\ g > 0$ $\varphi = -3.6°,\ g < 0$

Fig. 14. Gravity effect on simulated morphologies of hexane drying fronts, and corresponding saturations, for increasing drying times (liquid is black, vapor is white). Pore segments with square cross-section: (a) $g = 0$, (b) $g > 0$, and (c) $g < 0$.

we mean the combined process of moving liquid to the surface and evaporating it from there, by evaporation we mean liquid removal by internal evaporation. The compact front behind the rough is determined almost exclusively by evaporation. Liquid removal switches from drainage to evaporation after 2 h of drying and thus the fronts in the image sequence in the left column of Fig. 14 are all controlled by evaporation. The central column in Fig. 14 displays the corresponding sequence of saturation maps and drying fronts for the case $g > 0$. In this case drainage switches to evaporation after 2.4 h of drying and thus the fronts in the image sequence in the central column of Fig. 14 are all evaporation-controlled. The sequence shows that at any stage of the process a compact front forms which is determined almost exclusively by partial-pressure-gradient-driven evaporation. The rightmost column in Fig. 14 displays the corresponding sequence of saturation maps and drying fronts for the case $g < 0$. The sequence shows that at any stage of the process a rough front forms, dominated by long and initially weakly connected vapor fingers, which is determined almost exclusively by pressure-gradient-driven liquid flow. In this case drainage switches to evaporation after 1 h of drying, however enough to remove 57% of the liquid. The exact moment of the drainage-evaporation transition is captured in the second frame from the top of the rightmost column in Fig. 14.

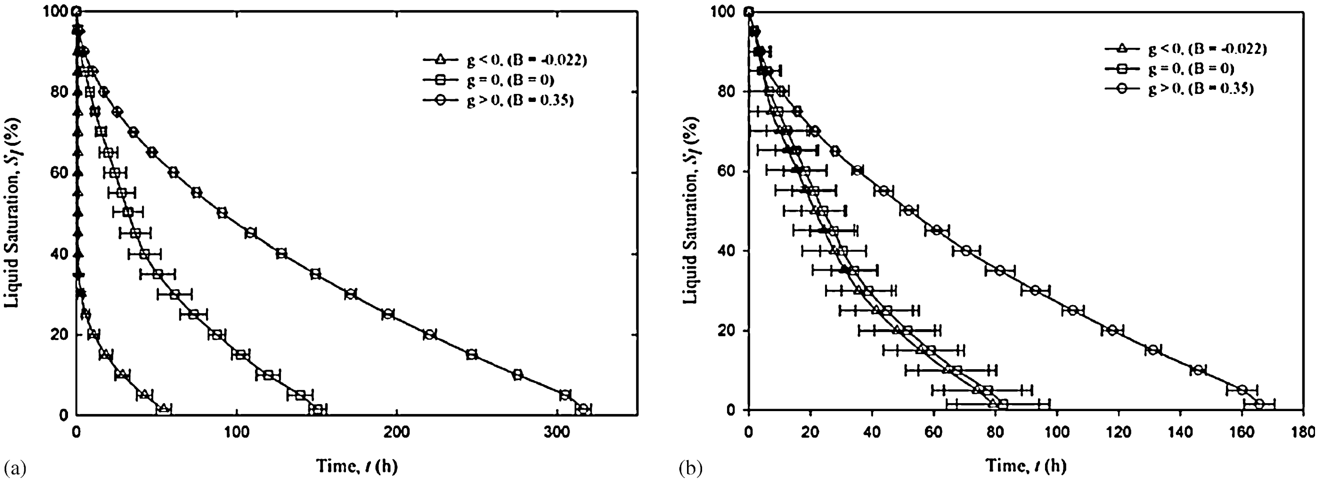

(a) (b)

Fig. 15. Gravity effect on simulated drying curves in pore networks saturated with hexane: (a) 2D 100 × 100 pore networks, (b) 3D 15 × 30 × 15 pore networks. Pore segments with square cross-section. Pore size distribution is shown in Fig. 4e.

The pronounced effect of gravity on drying rates, saturation distributions and drying front morphologies is clearly manifested also in the drying curves, liquid permeability and vapor diffusivity shown in Figs. 15 and 16. These results are also strongly dependent on the dimensionality of the embedding space, an aspect already discussed. For the 2D pore network, the transition from drainage to evaporation for the three cases of gravity was discussed around the results in Fig. 14. For the 3D pore network, for the case $g > 0$ drainage switches to evaporation quickly after 2.8 h of drying, drying is evaporation-controlled and is thus very slow as Fig. 15b shows; for the case $g < 0$ the switch is only after approximately 8 h of drying, after removing only about 30% of the liquid. Drainage time in 3D networks is significantly longer and removes less liquid than in 2D; drainage time is ultimately determined by evaporation from the outer surface of the large masses of liquid transferred by pumping.

Liquid hexane permeability in Fig. 16a and vapor hexane diffusivity in Fig. 16b from the 3D pore network show the expected trends, that is, as liquid content decreases liquid permeability decreases and vapor diffusivity increases. In all three cases of g, liquid permeability approaches the typical s-shaped form. The permeability of liquid hexane exhibits little sensitivity to network orientation at high liquid saturations. A strong liquid-saturated pore network exists. As liquid saturation decreases a pronounced spread of the liquid permeability is observed as the network orientation changes. Permeability decreases abruptly once mainly small-saturated pores and liquid wedges composed liquid saturation. As expected, this abruptness is more pronounced for the case $g > 0$. The inflection point in the permeability marks the point where wedges of liquid control its conductivity; at this point the liquid network is unable to sustain significant liquid flow. In all three cases of g, according to Fig. 16b, the vapor diffusivity approaches the inverted s-shaped form, rising abruptly once a sample-spanning cluster of hexane vapor is first established. Then diffusivity increases smoothly as liquid saturation decreases. As liquid saturation decreases, vapor diffusivity in-

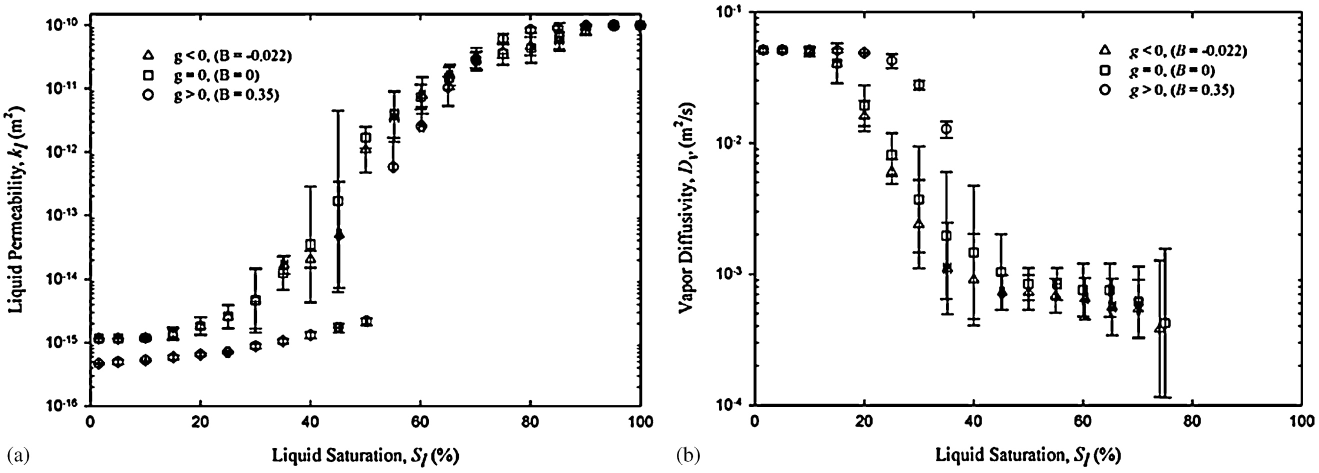

(a) (b)

Fig. 16. Gravity effect on: (a) liquid hexane permeability and (b) vapor hexane diffusivity in 3D 15 × 30 × 15 pore networks. Pore segments with square cross-section. Pore size distribution is shown in Fig. 4e.

creases slowly. For liquid saturations in the medium range, as large populations of pore segments become dry, the vapor diffusivity increases faster, abruptly in the $g > 0$ case. At low enough saturations, liquid hexane exists mainly as liquid wedges in pore corners; vapor diffusivity recovers a low increasing pace, as liquid wedges become thinner, before reaching its highest value which is insensitive to network orientation.

10. Conclusion

A mechanistic pore-level model of drying incorporating pressure-gradient-driven liquid flow and partial-pressure-gradient-driven evaporation in pore networks is used to determine pore-level distribution of vapor and liquid, drying curves, liquid permeability and vapor diffusivity as a function of liquid content. Sensitivities to embedding space, pore size distribution, pore shape and network orientation with respect to gravity are examined. Pore network dimensionality, pore size skewness, and variance to some extend, and negative gravity produced a pronounced effect on saturation distribution and drying parameters. Pore shape has a minor effect, except once saturation is mainly composed by thin liquid wedges.

Acknowledgments

We thank CONICYT of Chile for financial support through project FONDECYT No. 2990061. PGT thanks the Research Direction of University of Concepción for financial support through project DIUC 203.096.057-1.0. LS thanks University of Bío-Bío for sustained support.

References

[1] J.F. Daian, J. Saliba, Determination d'un réseau aleatoire de pores pour modéliser la sorption et la migration d'humidité dans un mortier de ciment, Int. J. Heat Mass Transfer 34 (8) (1991) 2081–2096.
[2] S.C. Nowicki, H.T. Davis, L.E. Scriven, Microscopic determination of transport parameters in drying porous media, Drying Technol. 10 (4) (1992) 926–946.
[3] M. Prat, Percolation model of drying under isothermal conditions in porous media, Int. J. Multiphase Flow 19 (4) (1993) 691–704.
[4] M. Prat, Isothermal drying of non-hygroscopic capillary-porous material as an invasion percolation process, Int. J. Multiphase Flow 21 (5) (1995) 875–892.
[5] J.B. Laurindo, Evaporation en milieu poreux, Etude expérimentale sur milieux-modeles et modélisation de type percolation, PhD Thesis, Institut National Polytechnique de Tolouse, France, 1996.
[6] J.B. Laurindo, M. Prat, Numerical and experimental network study of evaporation in capillary porous media. Phase distributions, Chem. Eng. Sci. 51 (23) (1996) 5171–5185.
[7] J.B. Laurindo, M. Prat, Numerical and experimental network study of evaporation in capillary porous media. Drying rates, Chem. Eng. Sci. 53 (12) (1998) 2257–2269.
[8] M. Prat, F. Bouleux, Drying of capillary porous media with a stabilized front in two dimensions, Phys. Rev. E 60 (5) (1999) 5647–5656.
[9] Y. Le Bray, M. Prat, Three-dimensional pore network simulation of drying in capillary porous media, Int. J. Heat Mass Transfer 42 (1999) 4207–4224.
[10] M. Prat, Recent advances in pore-scale models for drying of porous media, in: Proceedings of the 12th International Drying Symposium, Noordwijkerhout, The Netherlands, 2000.
[11] I.N. Tsimpanogiannis, Y.C. Yortsos, S. Poulou, N. Kanellopoulos, A.K. Stubos, Scaling theory of drying in porous media, Phys. Rev. E 59 (4) (1999) 4353–4365.
[12] A.G. Yiotis, A.K. Stubos, A.G. Boudouvis, Y.C. Yortsos, A 2-D pore-network model of the drying of single-component liquids in porous media, Adv. Water Res. 24 (2001) 439–460.
[13] T.M. Shaw, Movement of drying front in a porous material, Mater. Res. Soc. Symp. Proc. 73 (1986) 215–223.
[14] T.M. Shaw, Drying as an immiscible displacement process with fluid counterflow, Phys. Rev. Lett. 59 (1987) 1671–1674.
[15] L.A. Segura, P.G. Toledo, Pore-level modeling of isothermal drying pore networks., Evaporation and viscous flow, Latin Am. Appl. Res. 35 (2004) 43–50.
[16] L.A. Segura, P.G. Toledo, Pore-level modeling of isothermal drying of pore networks accounting for evaporation, viscous flow and shrinking, in: M.A. Silva, S.C.S. Rocha (Eds.), A.S. Mujumdar (Series Ed.), Proceedings of the 14th International Drying Symposium, vol. A, Sao Paulo, Brazil, 2004, pp. 733–741.
[17] D. Wilkinson, J.F. Willemsen, Invasion percolation: a new form of percolation theory, J. Phys. A: Math. Gen. 16 (1983) 3365–3376.
[18] W.B. Haines, Studies in the physical properties of soil—the hysteresis effect in capillary properties and the modes of moisture distribution associated therewith, J. Agric. Sci. 20 (1930) 97–116.
[19] C. Bustos, P.G. Toledo, Pore-level modeling of gas and condensate flow in two- and three-dimensional pore networks. Pore size distribution effects on the relative permeability of gas and condensate, Trans. Porous Media 53 (2003) 281–315.
[20] P.G. Toledo, L.E. Scriven, H.T. Davis, Pore-space statistics and capillary pressure curves from volume-controlled porosimetry, SPE Formation Eval. 9 (1) (1994) 46–54.
[21] M.J. Blunt, Effects of heterogeneity and wetting on relative permeability using pore level modeling, SPE J. 2 (1997) 70–87.
[22] R.G. Hughes, M.J. Blunt, Pore scale modeling of rate effects in imbibition, Trans. Porous Media 40 (3) (2000) 295–322.
[23] K. Mogensen, E. Stenby, S. Banerjee, V. Baker, Comparison of iterative methods for computing the pressure field in a dynamic network model, Trans. Porous Media 37 (1999) 277–301.